A&A 454, 277–286 (2006)
DOI: 10.1051/0004-6361:20064931

Astronomy & Astrophysics

UBVRI polarimetry of the massive interacting binary SX Cassiopeiae: modeling the electron-scattering circumstellar envelope⋆

V. Piirola[1,2], A. Berdyugin[1], G. V. Coyne, S. J.[2], Yu. S. Efimov[3], and N. M. Shakhovskoy[3]

[1] Tuorla Observatory, University of Turku, 21500 Piikkiö, Finland
e-mail: [piirola;andber]@utu.fi
[2] Vatican Observatory, 00120 Città del Vaticano
[3] Crimean Astrophysical Observatory, PO Nauchny, Crimea, 98409, Ukraine

Received 30 January 2006 / Accepted 28 February 2006

ABSTRACT

Aims. We perform a study of the structure, density, and distribution of ionized circumstellar gas in the strongly interacting binary SX Cas.
Methods. We apply our new model codes for electron scattering in circumstellar matter to analyze a previously unpublished, extensive linear polarization data set for SX Cas, collected during four successive observing periods in 1981–84 at the Crimean Astrophysical Observatory. These data are complemented by our polarization observations carried out in 2000 and 2005 with the KVA-60 telescope at La Palma.
Results. A clear, phase-locked pattern of polarization variations over the 36.6-day orbital period is revealed in each season, showing significant 1st and 2nd harmonic Fourier components and pronounced effects in the U and B bands at the primary eclipse, when the hot component and the surrounding circumstellar matter are obscured by the companion star. Seasonal variability is also found, but the major features of the polarization curves are well explained by a model with an extended scattering region on the trailing side of the accreting star, where the stream from the companion hits the accretion disk. No significant polarized flux is detected from the disk. We interpret this as being due to multiple scattering and strong absorption effects in the optically thick medium, which reduce the polarization of the light emerging from the disk to low levels. The modeled scattering region is above the orbital plane by about 10°, as seen from the center of the mass gainer. We attribute this to dominant electron scattering taking place on the upper side of an optically and geometrically thick accretion disk seen at an inclination $i \sim 78°$ by the observer.

Key words. polarization – stars: binaries: eclipsing – accretion, accretion disks – stars: individual: SX Cas – plasmas – scattering

1. Introduction

SX Cas is a member of a peculiar subset of interacting binary stars, also called W Serpentis type stars, according to the prototype of this class of long-period Algols. They are characterized by strong ultraviolet emission lines from highly ionized species (C IV 1550λ, Si IV 1400λ, N V 1240λ, etc.) and UV continuum with higher color temperature than deduced from the optical spectra (Plavec & Koch 1978; Plavec 1980; Weiland et al. 1995; Peters 2001).

W Ser type binaries are believed to be in or occur shortly after the rapid mass transfer phase. The large amount of circumstellar matter complicates the interpretation of the observed light and radial velocity curves, leaving significant uncertainties in the determination of the basic binary parameters, such as the radii and the spectral types of the component stars. This is well-demonstrated in the classic work on SX Cas by Struve (1944) and the long observational history thereafter (see e.g. Shao 1967; Koch 1972; Plavec et al. 1982; Andersen et al. 1988, and the references therein).

A significant step in understanding the properties of the hot mass-gaining object in SX Cas and other W Ser type systems was made in the work of Plavec et al. (1982), which combined IUE and optical spectra covering the wavelength interval 110–680 nm. The far-ultraviolet excess was explained by revising the earlier adopted spectral types (A6 III + G6 III) to B7 + K3 III. A considerable amount of continuous hydrogen radiation was found. This was associated with a disk seen edge-on, a view that explains also the strong line and continuous absorption of the light of the B7 star. The disk also substantially affects the shape of light curves (Pavlovski & Kříž 1985).

With the precise radial velocity curves obtained for the secondary star, Andersen et al. (1988) were able to refine the basic geometric configuration of SX Cas and explain the observed properties of the system with a consistent, semi-detached model. A rather drastic revision of the binary parameters was needed, resulting in a much larger secondary star radius and lower orbital inclination than adopted in the earlier published models. While Andersen et al. (1988) mainly focused on the two component stars, trying to avoid and eliminate the effects from the circumstellar matter, these authors also concluded that further study of the accreting material in the system was needed.

Linear polarization produced by scattering from free electrons carries important information about the density and distribution of circumstellar envelopes in binary stars. In particular,

⋆ Individual measurements (Tables 2 and 3) are only available in electronic form at the CDS via anonymous ftp to
cdsarc.u-strasbg.fr (130.79.128.5) or via
http://cdsweb.u-strasbg.fr/cgi-bin/gcat?J/A+A/454/277

Table 1. Summary of observations of SX Cas.

Year	HJD-2 400 000	Filters	Nights	*N* (obs)
1981	44 867.469–44 898.370	*UBVRI*	13	124
1982	45 185.502–45 301.360	*UBVRI*	29	252
1983	45 562.521–45 712.197	*UBVRI*	25	254
1984	45 948.441–46 000.391	*UBVRI*	18	142
2000	51 796.629–51 829.691	*UBVRI*	23	184
2005	53 636.447–53 695.432	*B*	16	64

the phase-locked pattern of polarization variations over the orbital cycle, and the changes during the eclipses of the primary star and the scattering material by the companion, are useful for developing plausible models of the system.

Evidence of polarimetric variability in SX Cas over the binary cycle has been given by Pfeiffer & Koch (1973, 1977). Elias (1990) has reported on his work to estimate the sizes of the SX Cas scattering regions and limits on their electron number density from polarimetry. There is evidence that the system passed from a "quiescent" to "chaotic" state between 1988 and 1989, most likely as the result of the variable mass transfer rate.

We have carried out extensive polarimetric observations of SX Cas to determine the short-term polarization modulation due to the orbital motion (36.6 d period) and to follow possible longer-term changes over successive observing seasons. The data provide solid basis for applying our new model codes for polarization effects from electron scattering in the circumstellar environment.

2. Observations

Long-term polarimetric monitoring of SX Cas was carried out at the Crimean Astrophysical Observatory (CRAO) in 1981–84 with the 1.25 m AZT-11 telescope and at the Observatorio del Roque de los Muchachos, La Palma, in 2000 with the 60 cm KVA telescope, using multichannel versions of the double-image-chopping polarimeter (Piirola 1973, 1988). These polarimeters allow us to measure linear polarization in the Johnson *UBVRI* bands simultaneously, by using dichroic filters to split the light into different spectral regions. The resulting passbands are close to the standard *UBVRI* system, with equivalent wavelengths of 0.36, 0.44, 0.54, 0.69, and 0.83 μm, respectively. The total integration time for one polarization phase bin (nightly mean point) was typically 30 min at the CRAO 1.25 m telescope and 1 hour at the KVA-60.

We also observed SX Cas, and surrounding field stars, in 2005 at the KVA-60. However, due to the severe forest fire in September and bad weather conditions in the fall of 2005, the amount of data obtained during this period is rather limited. The summary of observations is given in Table 1. Individual polarimetric observations are listed in Table 2 and photometric data in Table 3, available at the CDS.

The data at KVA-60 in 2005 were obtained in the fully remotely controlled mode of the telescope (operated from Tuorla), with the recently developed CCD polarimeter (DIPOL). This polarimeter is equipped with an Apogee AP47p camera with a Marconi CCD47-10, back-illuminated, thinned CCD that has a high blue sensitivity. It uses a rotating superachromatic half-wave plate as the retarder and a calcite plate as the analyzer. Two perpendicularly polarized stellar images, with a separation of 0.5 mm (11.5 arcsec), are produced on the CCD by the calcite plate. The intensities of these images are modulated by the rotating half-wave plate with an amplitude proportional to the degree of linear polarization of the incoming light. Double cosine curves, in antiphase for the *o*- and *e*-images, are observed over each revolution of the retarder.

For linear polarimetry, the retarder is rotated at 22.5° intervals between exposures, i.e., 16 exposures correspond to a full rotation of the retarder. One polarization measurement is obtained from every 4 exposures. For SX Cas, we typically made 16 exposures with 60 s integration time to obtain good statistical accuracy (±0.03%) and error control. A set of high-throughput broad-band filters with passbands close to the Johnson *UBVR* bands are provided in the filter wheel. The *B* filter was used for the CCD polarimetry of SX Cas.

Standard CCD reduction procedures (bias, dark, and sky subtraction; centroid determination) were applied to extract the flux of the two stellar images in each CCD frame. Least-square fits to each set of exposures provide the normalized Stokes parameters $q = Q/I = P_x = P\cos 2\theta$ and $u = U/I = P_y = P\sin 2\theta$ with good inherent stability, and also automatically eliminate the difference in the transmission coefficient for the *e*- and *o*-beams and any effects from atmospheric transparency variations (Piirola 1973).

Instrumental polarization was determined by observations of unpolarized nearby stars, with an uncertainty of <0.02% in each passband for the CRAO 1.25 m telescope, and was subtracted from the observed parameters q and u. For the KVA-60 telescope, the instrumental polarization was found to be negligible (<0.03%). The position angle calibration to the equatorial system was done by observing polarized standard stars.

3. Results and discussion

3.1. Photometry

Figure 1 shows our simultaneous *UBVRI* photometry of SX Cas from the CRAO 1.25 m telescope. The phases in Fig. 1 and throughout the present paper have been calculated with the ephemeris from Andersen et al. (1988):

$$T(\mathrm{min}) = \mathrm{HJD}\ 2\,446\,358.921 + 36.5610\,\mathrm{E},$$

which satisfactorily gives the times of the primary eclipse for our observing time interval. We do not have sufficient eclipse data in 2000 and 2005 to compute an improved ephemeris.

The light curves in Fig. 1 show strong color dependence. The depth of the secondary minimum (phase 0.5) increases, whereas the primary minimum (phase 0.0) decreases toward longer wavelengths. No clear secondary eclipse is seen in the *U* band, while the two minima are of nearly equal depth in the *I* band. The bottom of the primary eclipse is not flat, but the observed intensity continues to decrease during the totality. This suggests significant contribution to the observed flux from matter located on the trailing side of the primary, and gradually eclipsed toward the end of the totality of the eclipse of the primary star. Near the phases 0.7–0.8 the same cloud of material is in front of the primary, and the obscuration effects are responsible for the slightly (~0.05 mag) lower height of the second maximum in the light curves.

The color indices change to bluer colors at the secondary minimum, where the cooler companion is eclipsed, and to redder colors at the primary minimum, when the hot star is obscured by the companion. The behavior in the $(U - B)$ index is in contrast with that found in W Ser, where the $(U - B)$ index changes to *bluer* colors at the primary eclipse (Young & Snyder 1982; Guinan 1989; Piirola et al. 2005), indicating that redder

Table 4. The major axes, A_1 and A_2, of the 1st and 2nd harmonic ellipses, and the constant terms, q_o and u_o, from Fourier fittings to the *UBVRI* polarization data. Estimates of the orbital inclination, i, and the orientation angle (line of nodes), Ω, from BME78 models (2nd harmonic) are also given. The interstellar polarization components, q_{is} and u_{is}, are determined from the scattering model fittings (Sect. 4).

JD-2 400 000	Parameter	U	B	V	R	I
44 867–45 301	A_1(%)	0.30 ± 0.06	0.20 ± 0.04	0.12 ± 0.03	0.07 ± 0.02	0.09 ± 0.02
	A_2(%)	0.23 ± 0.06	0.17 ± 0.04	0.11 ± 0.03	0.06 ± 0.02	0.03 ± 0.02
	q_o(%)	0.36 ± 0.03	0.44 ± 0.01	0.36 ± 0.01	0.30 ± 0.01	0.27 ± 0.01
	u_o(%)	0.45 ± 0.02	0.46 ± 0.02	0.47 ± 0.01	0.43 ± 0.01	0.38 ± 0.01
	i(°)	85 ± 8	78 ± 7	72 ± 10	70 ± 13	89 ± 21
	Ω(°)	92 ± 8	87 ± 7	106 ± 12	61 ± 16	62 ± 17
45 562–46 000	A_1(%)	0.19 ± 0.06	0.21 ± 0.04	0.13 ± 0.03	0.10 ± 0.02	0.10 ± 0.02
	A_2(%)	0.26 ± 0.06	0.28 ± 0.04	0.16 ± 0.03	0.10 ± 0.02	0.06 ± 0.02
	q_o(%)	0.24 ± 0.03	0.31 ± 0.02	0.26 ± 0.01	0.24 ± 0.01	0.21 ± 0.01
	u_o(%)	0.39 ± 0.02	0.47 ± 0.02	0.48 ± 0.01	0.43 ± 0.01	0.39 ± 0.01
	i(°)	80 ± 7	77 ± 5	86 ± 5	68 ± 7	89 ± 10
	Ω(°)	106 ± 7	106 ± 5	98 ± 5	99 ± 10	106 ± 9
51 796–51 829	A_1(%)	0.16 ± 0.06	0.18 ± 0.05	0.12 ± 0.04	0.07 ± 0.02	0.19 ± 0.04
	A_2(%)	0.12 ± 0.06	0.13 ± 0.05	0.10 ± 0.04	0.05 ± 0.02	0.11 ± 0.04
	q_o(%)	0.20 ± 0.02	0.32 ± 0.02	0.30 ± 0.01	0.28 ± 0.01	0.20 ± 0.01
	u_o(%)	0.44 ± 0.02	0.45 ± 0.02	0.51 ± 0.02	0.46 ± 0.01	0.37 ± 0.01
	i(°)	100 ± 16	97 ± 12	91 ± 12	93 ± 12	95 ± 12
	Ω(°)	102 ± 15	92 ± 11	121 ± 11	84 ± 11	92 ± 10
44 867–46 000	q_{is}(%)	0.19 ± 0.02	0.28 ± 0.01	0.27 ± 0.01	0.25 ± 0.01	0.23 ± 0.01
	u_{is}(%)	0.45 ± 0.02	0.47 ± 0.01	0.49 ± 0.01	0.44 ± 0.01	0.39 ± 0.01

Table 5. Polarimetry and distances of field stars within 1° of SX Cas. See Sect. 3.3 for details.

Star	HD	Passband	P (%)	θ (°)	λ_{max} (μm)	d (pc)
1	232107	V	0.89 ± 0.03	50.0 ± 1.0		570
2	232108	B	0.78 ± 0.06	64.0 ± 2.0	0.584 ± 0.030	522
		V	0.85 ± 0.04	59.0 ± 1.2		
3	1027	B	0.51 ± 0.04	46.0 ± 2.0	0.569 ± 0.017	400
		V	0.56 ± 0.02	56.0 ± 1.0		
		R	0.53 ± 0.03	53.0 ± 2.0		
4	232104	V	0.75 ± 0.03	67.0 ± 1.3		488
5	232138	B	0.98 ± 0.05	58.0 ± 0.9	0.534 ± 0.012	960
		V	1.03 ± 0.03	65.0 ± 0.9		
		R	0.95 ± 0.06	62.0 ± 0.9		
6	246	V	0.99 ± 0.02	61.0 ± 0.7		407
7	232144	V	1.10 ± 0.03	56.0 ± 0.8		515
8	236298	V	0.52 ± 0.03	67.0 ± 1.7		573
9	232133	U	0.42 ± 0.03	55.6 ± 2.3	0.441 ± 0.007	≥62
		B	0.44 ± 0.02	58.2 ± 1.1		
		V	0.44 ± 0.02	58.1 ± 1.1		
		R	0.36 ± 0.01	56.0 ± 0.8		
		I	0.28 ± 0.01	57.7 ± 1.4		

parts of the optically thick envelope around the hot star are being eclipsed in W Ser. These differences illustrate that SX Cas shows a less extreme case of obscuration of the mass-gaining component by an optically thick circumstellar envelope. Some "blueing" can be seen in the color indices prior to and after the primary eclipse, but the sharp and deep primary minimum seen in all color indices resembles that due to an eclipse of a stellar-type object.

When compared with W Ser, the differences in binary and eclipse geometry between the two systems also have effects on the visibility of the circumstellar matter during the eclipse. Furthermore, in W Ser, the relative flux from the secondary star is very small, and the companion can only be seen from the obscuration effects on the flux from the primary. In SX Cas, the flux from the secondary star is significant in all of the *UBVRI* passbands, and it makes a substantial contribution to the observed color indices throughout the orbital cycle.

3.2. Polarimetry

Figure 2 shows our multi-waveband *UBVRI* polarimetry of SX Cas from the CRAO 1.25 m telescope. A sharp increase in polarization is seen in the U and B bands at the eclipse, when the diluting, unpolarized, direct light from the hot object is reduced. The circumstellar envelope is only partially obscured, and the scattering angles for the visible parts of the envelope are favorable for producing polarization. The scattering geometry also changes rapidly during ingress and egress.

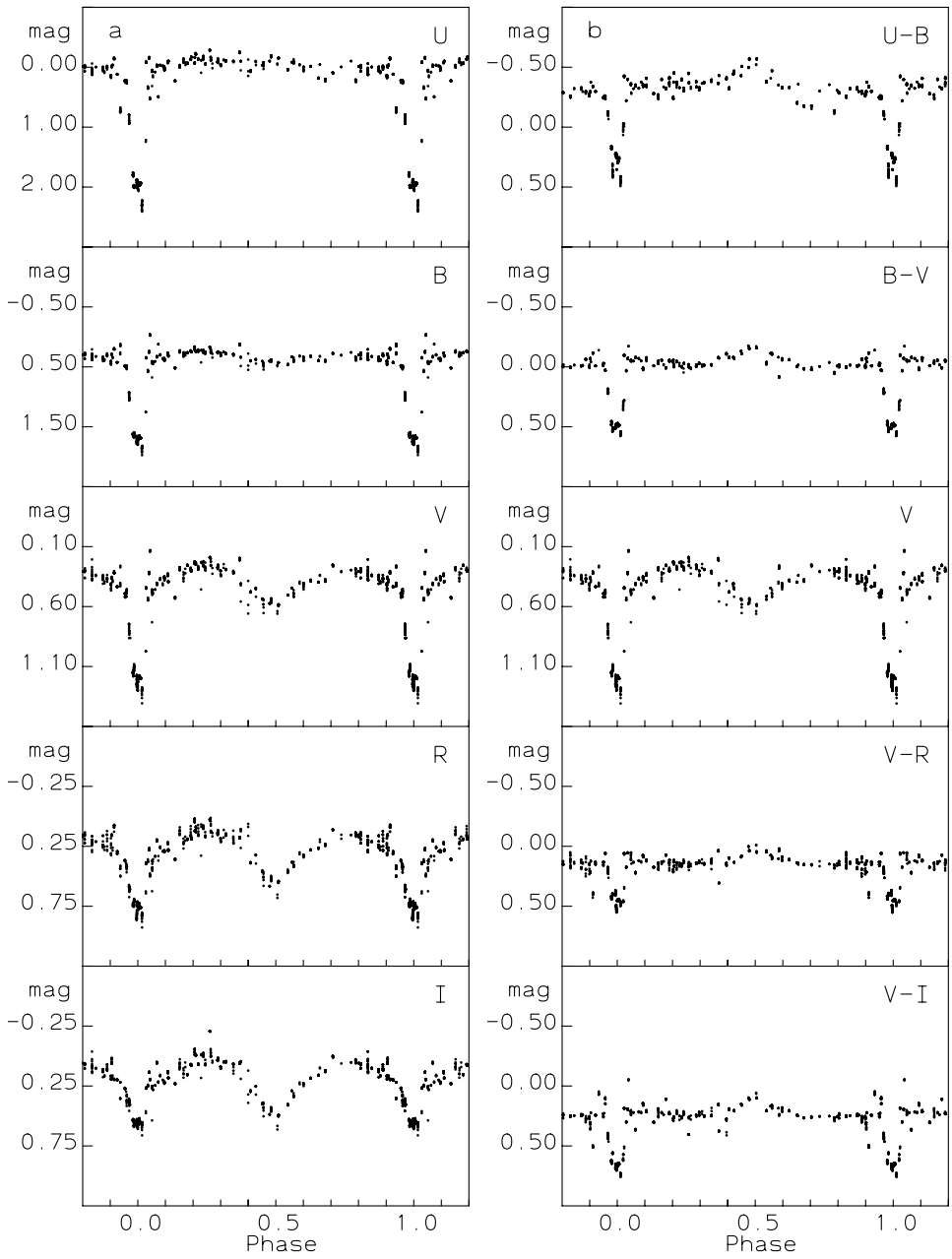

Fig. 1. a) *UBVRI* photometry of SX Cas relative to the comparison star BD + 54°0011. Note how the depth of the secondary minimum (phase 0.5) increases and the primary minimum (phase 0.0) decreases toward longer wavelengths. The magnitude scale in *U* and *B* is larger by a factor of two than that used in the other panels. **b)** The color indices change to bluer colors at the secondary eclipse and redder at the primary eclipse.

The range of peak-to-peak variations in the q parameter is about 1.5% in the U and ~0.8% in the B band. The parameter u shows smaller variations at the eclipse. In the V, R, and I bands the effects from the eclipse are only marginally seen, and the pattern of polarization variations more closely follows the sinusoidal 2nd harmonic curve typical for the phase-locked polarization curves found in binary stars.

Statistically significant 1st and 2nd harmonic Fourier components were clearly detected in each of the four observing seasons, though the data coverage obtained over the 36-day orbital period was not optimal for each individual season. To improve the *S/N* ratio, we have grouped the data here into two parts, combining the first two observing seasons (JD 2 444 867-5301) and the last two observing seasons (JD 2 445 562-6000) to illustrate the long term variability in polarization. Fourier fitting curves with first and second harmonics included are also shown for these two intervals in Fig. 2. While the main features of the polarization variations over the binary cycle are similar in both data sets, long-term changes have also taken place over the 4-year total monitoring period at CRAO.

For binary star polarization, the second harmonic usually is strongest, as predicted by the analytic scattering models (Brown et al. 1978 = BME78) for circumstellar material that is symmetric about the orbital plane. Our data for SX Cas show also a clear *first* harmonic, indicating that there is a significant contribution of scattered light coming from a region outside of the orbital plane, thus breaking the symmetry of the scattering envelope about the orbital plane.

To quantify the phase-locked polarization variability in the *UBVRI* bands, we list the amplitudes of the 1st and 2nd harmonics from the Fourier fittings in Table 4. The estimates of the orbital inclination, i, and the orientation of the line of nodes, Ω, from the BME78 models (2nd harmonic) are fairly consistent in different wavebands. The formal uncertainties of i and Ω have been calculated with the propagation of errors and the least-squares method. However, the BME78 models assume that

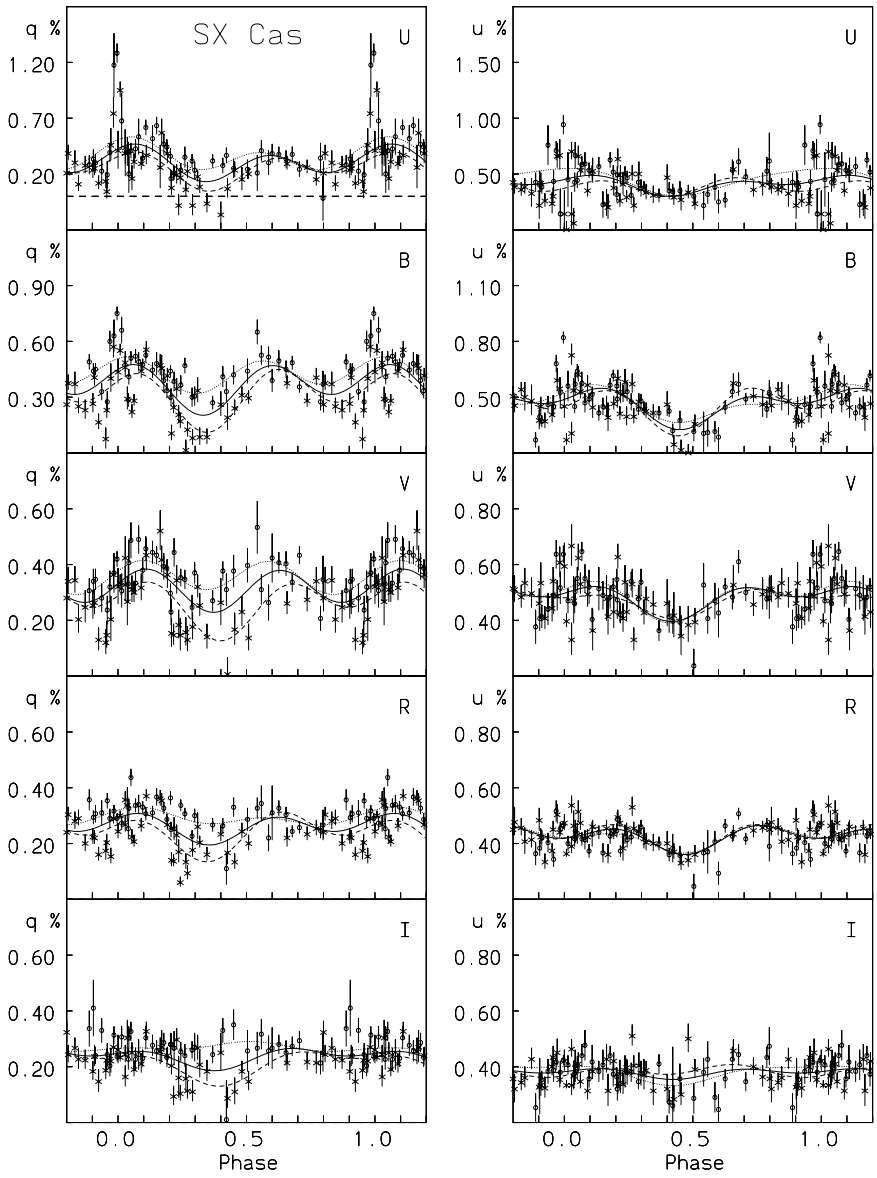

Fig. 2. *UBVRI* polarimetry of SX Cas in the intervals JD 2 444 867-5301 (dots) and JD 2 445 562-6000 (crosses), expressed in terms of the normalized Stokes parameters $q = P\cos 2\theta$ and $u = P\sin 2\theta$. Nightly mean points with standard error bars ($\pm\sigma$) are plotted against the (36.6 day) orbital phase. Second order Fourier fitting curves are also shown with dotted and dashed lines for the two intervals, respectively. The solid line gives a fit for the combined data set.

no obscuration effects take place (point-like stars), and should be applied with caution for eclipsing systems like SX Cas and W Ser (Piirola et al. 2005).

The amplitude of the 2nd harmonic polarization modulation is the largest in the *U* band and decreases significantly towards the *V*, *R*, and *I* bands. The reduction of the degree of polarization at longer wavelengths is typical of early-type stars surrounded by ionized disks/envelopes (see e.g. Poeckert & Marlborough 1978; Poeckert et al. 1979). Thomson scattering by free electrons is independent of wavelength, but the observed degree of polarization is lowered by self-absorption in the circumstellar medium, overlying emission in the UV, optical, and near-IR, and unpolarized free-free emission towards the infrared from a relatively large volume surrounding the system. The relative amount of unpolarized flux from the stellar components at different wavelengths also contributes to the observed polarization, and the cool companion star in SX Cas adds significant flux to the system, particularly in the *V*, *R*, and *I* bands, where the secondary star is brighter than the primary.

Some long-term polarization variability may be seen from the amplitudes of the 1st and 2nd harmonic Fourier terms shown in Table 4. In 2000 (JD 51 796-829), the amplitudes in *U* and *B* are smaller than in 1981–84 (JD 44 867–46 000). The *B*-band data we obtained in 2005 give $A_1(\%) = 0.21 \pm 0.05$, and $A_2(\%) = 0.18 \pm 0.05$, and the orbital phase dependence of polarization in accordance with the earlier observations at CRAO.

3.3. Interstellar polarization

To estimate interstellar polarization in the direction of SX Cas, we also observed 8 field stars within 1° of SX Cas, in the distance range 400–960 pc, using the KVA-60 telescope and the CCD polarimeter (Table 5). The *V* filter was used, as interstellar typically peaks in this wavelength region. The stars Nos. 2, 3, and 5 were also observed in *R* and/or *B* passbands to estimate the wavelength of the maximum interstellar polarization ($\lambda_{\max}$) from the modified Serkowski law (Whittet et al. 1992). Star No. 9 is the photometric comparison star observed during the *UBVRI* polarimetry, and these measurements also provide the polarimetric data in the *UBVRI* bands given in Table 5 for this star.

Since no *Hipparcos* parallaxes are available for the field stars in the distance range of interest, we made photometric distance estimates assuming the main sequence star luminosity and the normal reddening law. Taking the observed amount of

Table 6. Model fittings to the *UBVRI* polarization data. The total number of scattering electrons is approximated by $N_e \sim W \times 10^{46}$.

Parameter	*U*	*B*	*V*	*R*	*I*
W(1981-84)	8.3 ± 0.8	7.8 ± 0.8	5.7 ± 1.2	5.9 ± 1.3	3.0 ± 1.8
W(2000)	2.8 ± 1.9	2.5 ± 1.9	3.3 ± 1.8	1.9 ± 1.8	1.4 ± 3.0
Ω (°)	78.8 ± 1.9	85.2 ± 2.1	81.6 ± 2.6	74.3 ± 2.6	77.6 ± 2.8
q_{is}(%)	0.19 ± 0.02	0.28 ± 0.01	0.27 ± 0.01	0.25 ± 0.01	0.23 ± 0.01
u_{is}(%)	0.45 ± 0.02	0.47 ± 0.01	0.49 ± 0.01	0.44 ± 0.01	0.39 ± 0.01
p_{is}(%)	0.49 ± 0.02	0.56 ± 0.01	0.56 ± 0.01	0.50 ± 0.01	0.45 ± 0.01
θ_{is} (°)	33.6 ± 1.4	29.7 ± 0.7	30.4 ± 0.6	30.4 ± 0.8	29.5 ± 0.7

polarization for each star into account, these assumptions seem to be valid, except for star No. 9, where the resulting distance $d \sim 62$ pc (Table 5) appears too small compared with the observed degree of polarization, $P_B \sim 0.44 \pm 0.02\%$. Stars Nos. 3, 4, 6, 7, and 8 were also included in the *UBV* photometric survey of SX Cas field stars by Koch (1972), and his distance estimates are in reasonable agreement with ours, except for those of stars Nos. 6 and 8, for which the distances derived by Koch (1972), $d \sim 1.8$ kpc, and $d \sim 2.6$ kpc, respectively, are too large when compared with the amounts of polarization observed. Therefore, we have adopted the distance estimates given in Table 5.

Linear unweighted regression of the (P_V, d) values in Table 5 (excluding star No. 9, which is at an uncertain distance) yields a relation $P_V\% = (1.42 \pm 0.02)d$ kpc^{-1}. With the distance estimate for SX Cas, $d = 530 \pm 75$ pc (Andersen et al. 1988), the corresponding estimate of the value of interstellar polarization for SX Cas from the surrounding field stars is $P_V = 0.75 \pm 0.11\%$. The relatively smooth field direction (Fig. 3) and the well-aligned polarization vectors give the average position angle $\langle\theta_{is}\rangle = 60° \pm 2°$ for the interstellar polarization in the SX Cas field.

There is a 12th magnitude F5V star, AC+55°249, only 17″ from SX Cas and at a distance of $d = 450 \pm 60$ pc, very close to that derived for SX Cas itself by Andersen et al. (1988), who suggested a possible physical connection between the stars. Because of the relative faintness of AC + 55°249 for polarimetry with a 60 cm telescope, we observed the star in white light, and found $P = 0.32 \pm 0.03\%$. This is about half of what is predicted by the (P_V, d) relation determined above. Only part of the discrepancy is explained by the broad wavelength range included in the white light measurement. Also, the position angle $\theta = 35° \pm 3°$ differs by ∼25° from the average value $\langle\theta_{is}\rangle = 60°$ found for the field stars. We will discuss the estimates of the interstellar polarization component of SX Cas in more detail in Sect. 4, together with the results from the model fittings.

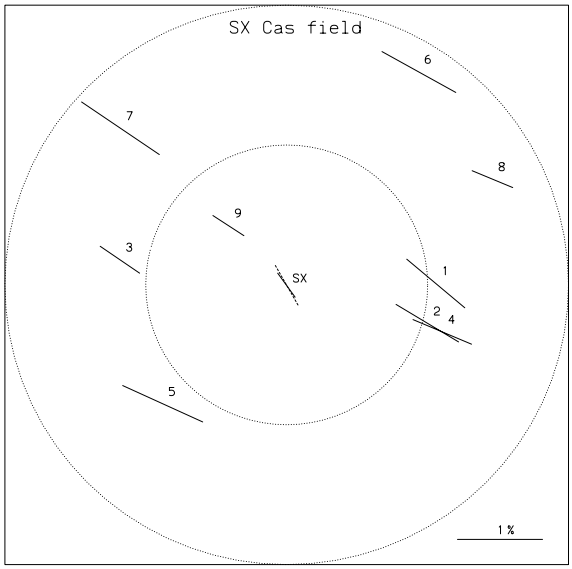

Fig. 3. Map of *V*-band polarizations of field stars around SX Cas. The circles centered on SX Cas have radii 0.5° and 1.0°. The solid line labeled SX gives the polarization of the visual companion of SX Cas (in white light), and the dashed line gives the interstellar polarization of SX Cas in the *V* band, derived from our scattering model fittings. North is up and east to the left. The length of the line in the lower right corner corresponds to 1% degree of polarization.

4. Model computations

To simulate polarization effects from scattering by free electrons (Thomson scattering) in the circumstellar environment of binary stars, we developed numerical integration codes, taking into account the finite size of the illuminating sources and the eclipse effects from two spherical stars (Piirola 1980). These models were recently further developed, and more sophisticated fitting algorithms were also implemented. A detailed account of the modeling routines was given in Piirola et al. (2005).

As initial values of the binary system parameters for SX Cas, we adopted the relative radii of the stellar components, $r_1 = 0.035 \pm 0.004$, $r_2 = 0.27 \pm 0.01$ (in units of the binary separation, $a = 1$), and the orbital inclination, $i = 78.7° \pm 0.5°$, from Andersen et al. (1988). Depending on the distribution of the scattering material, model fittings to the polarization curves may provide further constraints, in particular on the orbital inclination.

To calculate the normalized Stokes parameters $q = Q/I$ and $u = U/I$, we adopted $I = I_{obs}$, where I_{obs} is the observed intensity as a function of the orbital phase. I_{obs} takes into account the variability of the unpolarized total flux outside the eclipses. This is mainly due to the ellipticity of the secondary star, which has a major contribution in the light curves, particularly in the *V*, *R*, and *I* passbands.

Scattering points are distributed around the primary star in the form of various components, such as a spherical shell, a disk of a given thickness, a scattering spot/cloud at latitude ϕ_{sp} and longitude λ_{sp}, with opening angles $\triangle\phi$ and $\triangle\lambda$, respectively. The cloud is radially confined between inner and outer distances (r_{in}, r_{out}) from the center of the primary. A stream between the two stars is included, with a variable angle from the line joining the two stars.

To fit the scattering model, we grouped the data into 100 normal points in each color band (Figs. 4–7), representing the average polarization behaviour of SX Cas and the corresponding distribution of the scattering material over the 4-year time interval, 1981–84. There are some long-term variations (Fig. 2 and Table 4), but the main features in the polarization curves remain similar in each season. Therefore, we consider the use of the

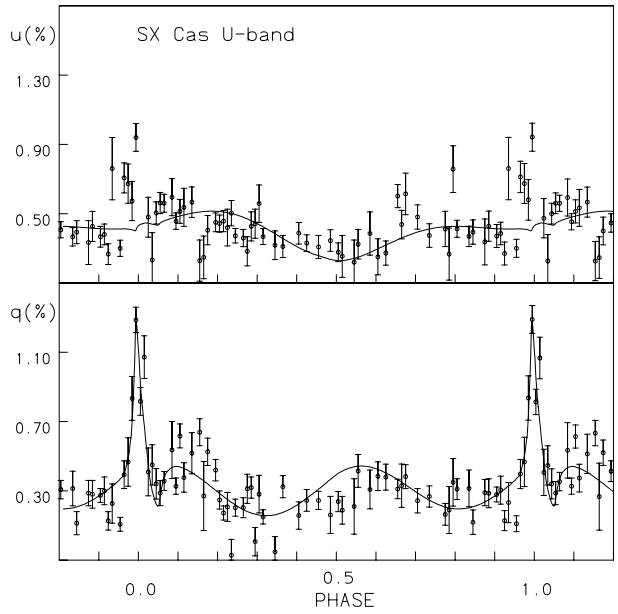

Fig. 4. *U* band polarimetry of SX Cas. Independent phase bins (1/100 phase interval) computed from the CRAO 1981–84 data are shown with $\pm\sigma$ error bars and model-fitting curves (see Sect. 4).

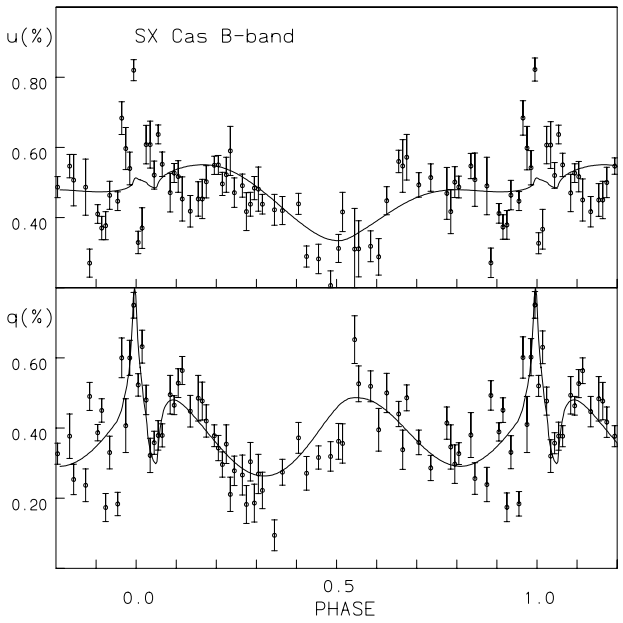

Fig. 5. The same as in Fig. 4 in the *B* band.

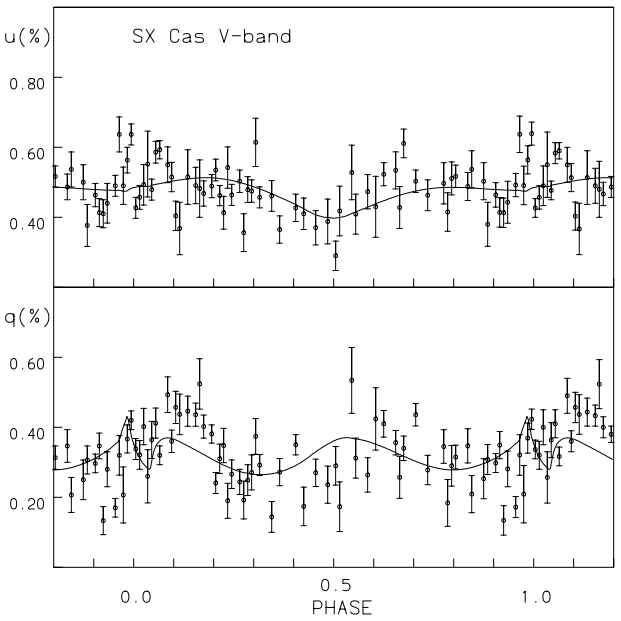

Fig. 6. The same as in Fig. 4 in the *V* band.

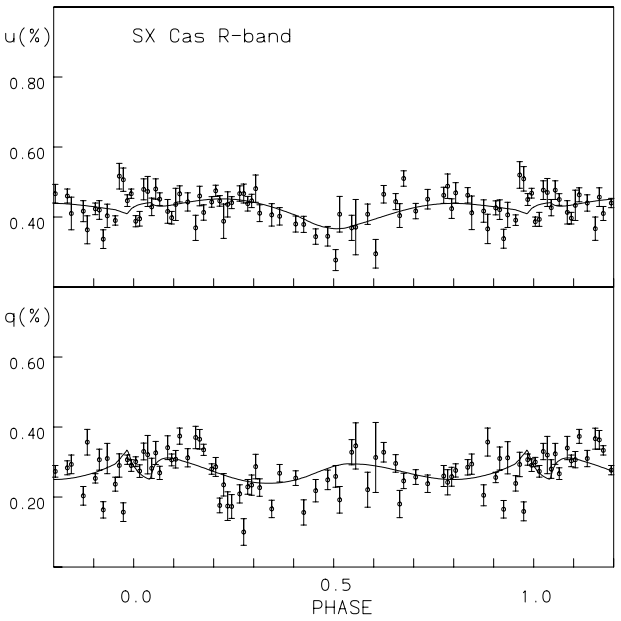

Fig. 7. The same as in Fig. 4 in the *R* band.

average curves appropriate, for the sake of brevity and the purposes of the present paper.

Just as in the case of W Ser (Piirola et al. 2005), we have found no evidence of a scattering disk in SX Cas from the polarization curves, i.e., the disk (or ellipsoidal envelope) component in the model fittings is not statistically significant. It is most likely that the disk is optically thick and has a well-defined visible pseudophotosphere. Multiple scattering and strong absorption effects in the optically thick medium reduce the polarization of the light emerging from the disk to low levels.

Unlike in W Ser, no statistically significant spherical shell or stream components are seen in SX Cas from our data. There are some deviations of the observed points from the model curves in the parameter *u* at the primary eclipse (Figs. 4, 5), indicating a possible vertical structure of the matter (away from the orbital plane) in the vicinity of the primary. However, these features are too transient to be explained by our present model. The fittings provide an upper limit of about $n_e < 10^{11}$ cm^{-3} for the electron density in an optically thin scattering spherical shell around SX Cas. This is consistent with the conclusions from earlier photometric and spectroscopic studies, which indicate that SX Cas is a "cleaner" system than W Ser, with the mass-gaining star less obscured by a circumstellar envelope than in W Ser. Due to the absence of a spherical shell component, our polarization model does not put better constraints on orbital inclination than obtained by Andersen et al. (1988), but further supports its value being near $i \sim 78° \pm 1°$.

Our polarimetry and model fittings reveal with good statistical significance ($S/N \sim 10$ in the *U* and *B* bands) an extended scattering cloud/region on the trailing side of the primary star, where the accretion stream hits the accretion disk, although we

do not see the stream itself from the present polarization data. Figures 4–7 show the polarization curves from the model fittings, together with the observations in the *UBVR* bands. An eclipse structure is seen in the parameter q, particularly prominent in the U and B bands. The polarization peaks sharply before the mid-eclipse, indicating that the scattering volume is still visible when the primary star is already eclipsed and the unpolarized direct flux is at minimum. The degree of polarization drops to smaller values after the mid-eclipse, when the the cloud of material above the trailing side of the primary is occulted by the secondary star. Another peak is seen in the q parameter curves near the phase 0.55, where the cloud is at maximum elongation on the other side of the primary.

The location and dimensions of the scattering cloud are determined from the U and B band data, which have the highest *S/N* ratio, and we have obtained $\lambda_{sc} \sim 71° \pm 3°$ and $\phi_{sc} \sim +10° \pm 2°$. The phase resolution over the eclipse is rather coarse, but the shape of the eclipse curve in the q parameter puts some constraints on the radial extension of the cloud. In units of the radius of the primary star, we have found the value $r_{in} \sim 2.5 \pm 0.5$, for the distance from the inner surface of the cloud to the primary star center. The outer radius r_{out} is not very strongly constrained, as the scattered flux from the cloud decreases with the increasing distance from the illuminating star. The slope of the decrease in the q-parameter after the mid-eclipse suggests that $r_{out} > 6$.

For a mass ratio $m_2/m_1 = 0.3$ (Andersen et al. 1988), the radius of the Roche lobe around the primary is $r_{RL} \sim 0.28a$, from the approximation formula given by Paczyński (1971). In units of the primary star radius, this gives $r_{RL} \sim 8$. For our computations, we have assumed the outer radius of the cloud, $r_{out} = 7.0$, which is about 88% of the radius of the Roche lobe. The opening angle of the cloud in longitude is not strongly constrained, and our model fittings give $\triangle\lambda = 40° \pm 30°$.

It is interesting to note that the scattering cloud is not located in the orbital plane, but above it by the angle $\phi \sim 10°$, as seen from the primary star center. This asymmetry comes from the *first* harmonic of the phase-locked polarization curves. In the view of the assumption that an optically and geometrically thick disk surrounds the primary, it is tempting to interpret the observed asymmetry as being due to dominant scattering taking place on the upper side of the opaque disk seen at an inclination of about $i \sim 78°$.

Table 6 lists the fitted model parameters derived from our data in the *UBVRI* bands for the model of the scattering cloud described above. The dimensionless numbers W given are proportional to the total number of scattering electrons in the respective component (see Piirola et al. 2005, for details). The decrease of the weighting factor W toward longer wavelengths is in accordance with self-absorption and overlying emission effects in the circumstellar medium, and dilution of the observed degree of polarization by unpolarized free-free emission, which are not included in our model. The wavelength dependence of W resembles that of Be-star polarization, except that no drop of polarization in the U-band is seen. Early-type stars with circumstellar disks typically show reduced polarization values shortwards of the Balmer jump, due to continuous Balmer absorption. The relatively strong polarization and correspondingly large value of W in the U band may also indicate some contribution from additional hot continuum scattered by the cloud, and possibly associated with the accretion stream impact region on the outer side of the disk.

The results from the 2000 data in Table 6 show SX Cas in a much less active state than in 1981–84. The electron number factors, W, are smaller by a factor of about 3, and the scattering

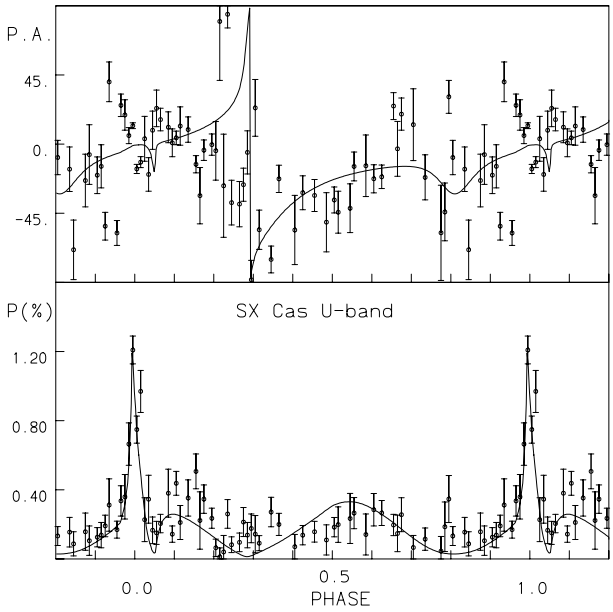

Fig. 8. Intrinsic polarization and position angle of SX Cas in U.

cloud is only marginally detected from the lower *S/N* data obtained by the KVA-60 telescope for this season.

The values for the position angle of the orbital plane projected on the sky (line of nodes), Ω, and the normalized Stokes parameters of the interstellar polarization from the model fittings, q_{is} and u_{is}, are listed in Table 6. The values of Ω obtained in different wavebands are reasonably consistent, and give a weighted average value $\langle\Omega\rangle = 79.5° \pm 1.8°$. The degree of interstellar polarization $p_{is}(\lambda)$, computed from (q_{is}, u_{is}) in different wavebands (Table 6), very closely follows the modified Serkowski law (Whittet et al. 1992), and gives $p_{max} = 0.568 \pm 0.004\%$, $\lambda_{max} = 0.528 \pm 0.008$ μm, with average position angle $\langle\theta_{is}\rangle = 30.6 \pm 0.5°$. The good agreement of $p_{is}(\lambda)$ with the wavelength dependence of the standard interstellar polarization law gives further evidence that the values of (p_{is}, θ_{is}) derived from our model fittings are nearly correct.

The position angle, θ_{is}, for SX Cas deviates by about 30° from the average field direction, $\langle\theta\rangle \sim 60°$, derived from the surrounding stars (Fig. 3). The visual companion AC+55°249, which is only 17″ from SX Cas, however, has $\theta = 35° \pm 3°$, in good agreement with the value of θ_{is} found for SX Cas from our scattering model fittings (Table 6 and Fig. 3). Accordingly, there seem to be some local disturbances in the otherwise rather smooth interstellar magnetic field direction. More data on the field stars would be needed to establish a possible connection between such deviations of the field direction and the star-forming region where SX Cas was formed.

Intrinsic polarization p_{in} and position angle θ_{in}, obtained by subtracting the derived interstellar polarization (q_{is}, u_{is}) from the observed parameters (q, u) of SX Cas, are shown in Figs. 8–11 for the *UBVR* bands. The intrinsic polarization goes close to zero at phase 0.3, where the scattering cloud is behind the primary star, and although the cloud is mostly visible, the average scattering angles are ∼0°. Another polarization minimum is observed near phase 0.8, where the cloud is in front of the primary, and average scattering angles are ∼180°. The position angle shows a rapid rotation near phase 0.3, where the polarization approaches zero. Smoother variations take place over the orbital cycle. They represent the first harmonic due to the asymmetry of the scattering region with respect to the orbital plane, i.e., $\phi_{sc} \sim 10°$.

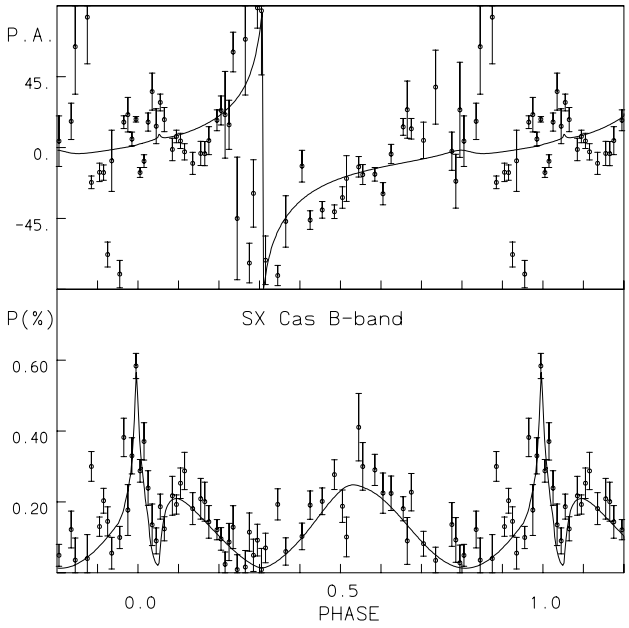

Fig. 9. Intrinsic polarization and position angle of SX Cas in *B*.

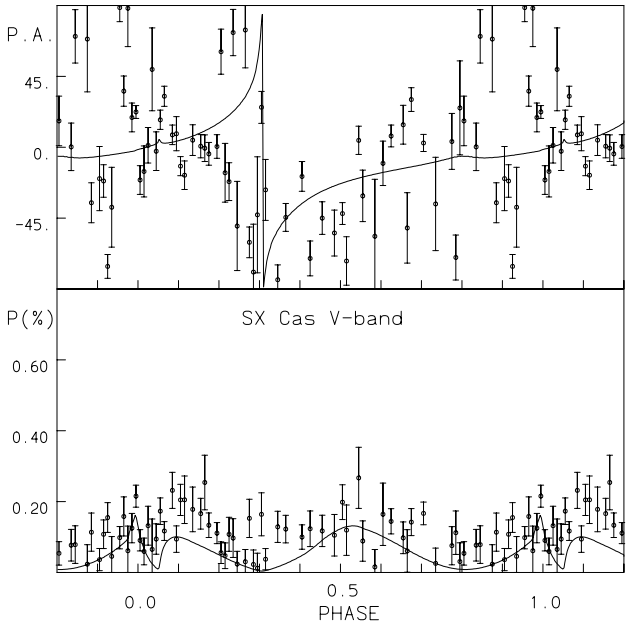

Fig. 10. Intrinsic polarization and position angle of SX Cas in *V*.

Obviously, the detailed structure of the circumstellar matter is more complicated than in the model applied, as indicated by the deviations of the observed points from the model curves.

Figures 12, 13 give illustrations of the model. They are true pictures of the scattering points, as seen at different orbital phases. Only the number of points shown is greatly reduced for clarity. The modeled scattering cloud is on the trailing side of the primary star, and above the orbital plane by 10°, as seen from the center of the primary star.

The accretion stream and the optically thick disk are shown schematically in the figures, although they are not detected from the present polarization data. The stream is drawn in the orbital plane, and the disk is symmetric about it. Points on the surface of the stellar components are added to show them in the pictures. No scattering envelopes are assumed there in the model computations.

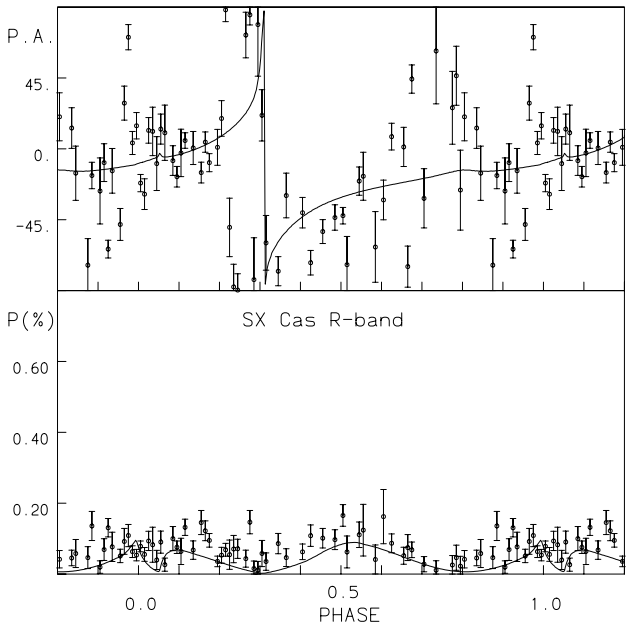

Fig. 11. Intrinsic polarization and position angle of SX Cas in *R*.

5. Conclusions

We collected an extensive multiwaveband (*UBVRI*) linear polarization data set for SX Cas. Clear polarization variations were detected over the orbital cycle, showing significant 1st and 2nd harmonic components and pronounced effects in the *U* and *B* bands at the primary eclipse, when the hot component and the surrounding circumstellar matter are obscured by the companion star.

We applied our new model codes for electron scattering in a circumstellar environment and found that the major features of the phase-locked polarization pattern are explained by a scattering cloud of free electrons on the trailing side of the primary star, where the stream from the companion hits the accretion disk. Eclipse effects in polarization constrain the radial extension of the cloud from the primary star. In units of the primary star radius, the scattering region is found to be confined between distances $r_{\rm in} \sim 2.5$ to $r_{\rm out} > 6$ from the center of the primary star, possibly extending up to, and even beyond, the radius $r_{\rm RL} \sim 8$ of the Roche lobe.

The decrease of polarization variation amplitude towards longer wavelengths is consistent with dilution effects from the unpolarized radiation of the cooler companion star and free-free emission from the circumstellar/binary matter. Self-absorption and overlying emission effects in the circumstellar medium also contribute. The relatively strong polarization in the *U* band indicates that either the effects from continuous Balmer absorption shortward of the Balmer jump are small, or there is some additional contribution from a hot continuum, possibly associated with the accretion stream impact region on the outer side of the disk.

As in the case of W Ser, we find no polarized flux from a disk-type component around the mass-gaining star in SX Cas. We interpret this as being due to the fact that the massive disk has a well-defined pseudophotosphere and that multiple scattering in the optically thick medium reduces the polarization of the light emerging from the disk to a low level.

The first harmonic of the phase-locked polarization variations indicates that the scattering region is not symmetric about the orbital plane, but is at latitude $\phi \sim 10°$ above the orbital

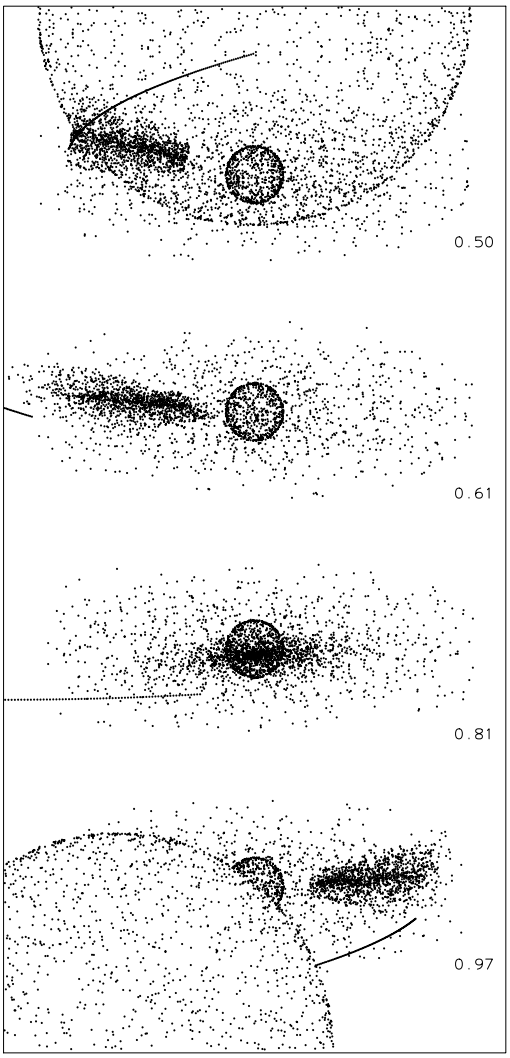

Fig. 12. Illustration of the model of scattering points, as seen at orbital phases 0.50–0.97. See Sect. 4 for details.

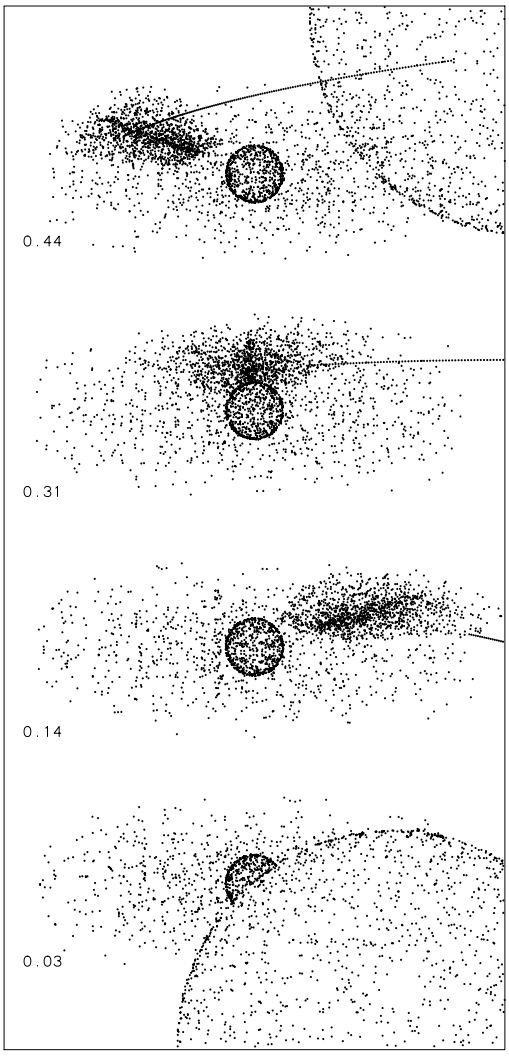

Fig. 13. Illustration of the model of scattering points, as seen at orbital phases 0.03–0.44. See Sect. 4 for details.

plane. We attribute this to dominant scattering taking place on the upper side of an optically and geometrically thick accretion disk seen at an inclination $i \sim 78°$ by the observer. No clear evidence is found from the present polarization data for a spherical shell around the primary or mass outflow in the polar directions.

Our results from multicolor polarimetry have provided complementary information on the geometry of the scattering circumstellar matter in SX Cas, not obtained from spectroscopy or photometry. The model developed shows a picture of a "cleaner" system with the mass-gaining primary less obscured by the circumstellar matter than in W Ser.

Acknowledgements. The work has been supported by research grants from The Academy of Finland for visits to the Crimean Astrophysical Observatory (CRAO). We thank the CRAO staff for their kind hospitality. The KVA-60 telescope is operated by Tuorla Observatory of the University of Turku, on the island of La Palma, in the Spanish Observatorio del Roque de los Muchachos (ORM) of the Instituto de Astrofisica de Canarias, under the agreement between the University of Turku, Finland, and the Royal Academy of Sciences, Sweden (Kungliga Vetenskapsakademien).

References

Andersen, J., Nordström, B., Mayor, M., & Polidan, R. S. 1988, A&A, 207, 37
Brown, J. C., McLean, I. S., & Emslie, A. G. 1978, A&A, 68, 415
Elias, N. M. 1990, Bull. A&AS, 22, 1334
Guinan, E. F. 1989, Space Sci. Rev., 50, 35
Koch, R. H. 1972, AJ, 77, 500
Paczyński, B. 1971, ARA&A, 9, 183
Pavlovski, K., & Kříž, S. 1985, Bull. Astron. Inst. Czechosl., 36, 153
Peters, G. J. 2001, in The influence of binaries on stellar population studies, ed. D. Vanbeveren (Dordrecht: Kluwer Academic Publishers), Astrophysics and Space Science Library (ASSL), 264, 79
Pfeiffer, R. J., & Koch, R. H. 1973, Inf. Bull. Var. Stars, No. 780
Pfeiffer, R. J., & Koch, R. H. 1977, PASP, 89, 147
Piirola, V. 1973, A&A, 27, 383
Piirola, V. 1980, A&A, 90, 48
Piirola, V. 1988, in Polarized Radiation of Circumstellar Origin, ed. G.V. Coyne, et al. (Univ. of Arizona Press), 735
Piirola, V., Berdyugin, A., Mikkola, V., & Coyne, G. V. 2005, ApJ, 632, 576
Plavec, M. J. 1980, in Close Binary Stars: Observations and Interpretations, ed. M. J. Plavec, D. M. Popper, & R. K. Ulrich (Dordrecht: Reidel), IAU Symp., 88, 251
Plavec, M. J., & Koch, R. H. 1978, Inf. Bull. Var. Stars, No. 1482
Plavec, M. J., Weiland, J. L., & Koch, R. H. 1982, ApJ, 256, 206
Poeckert, R., & Marlborough, J. M. 1978, ApJS, 38, 229
Poeckert, R., Bastien, P., & Landstreet, J. D. 1979, AJ, 84, 812
Shao, C.-Y. 1967, AJ, 72, 480
Struve, O. 1944, ApJ, 99, 89
Weiland, J. L., Shore, S. N., Beaver, E. A., Lyons, R. W., & Rosenblatt, E. I. 1995, ApJ, 447, 401
Whittet, D. C. B., Martin, B. G., Hough, J. H., et al. 1992, ApJ, 386, 562
Young, A., & Snyder, J. A. 1982, ApJ, 262, 269